Detection of Extended X-Ray Emission around the PeVatron Microquasar V4641 Sgr with XRISM

Hiromasa Suzuki[1], Naomi Tsuji[2,3], Yoshiaki Kanemaru[1], Megumi Shidatsu[4], Laura Olivera-Nieto[5], Samar Safi-Harb[6], Shigeo S. Kimura[7,8], Eduardo de la Fuente[9], Sabrina Casanova[10], Kaya Mori[11], Xiaojie Wang[12], Sei Kato[13,29], Dai Tateishi[14], Hideki Uchiyama[15], Takaaki Tanaka[16], Hiroyuki Uchida[17], Shun Inoue[17], Dezhi Huang[18], Marianne Lemoine-Goumard[19], Daiki Miura[1,14], Shoji Ogawa[1], Shogo B. Kobayashi[20], Chris Done[21], Maxime Parra[22,23], Maria Díaz Trigo[24], Teo Muñoz-Darias[25,26], Montserrat Armas Padilla[25,26], Ryota Tomaru[27], and Yoshihiro Ueda[28]

[1] Institute of Space and Astronautical Science (ISAS), Japan Aerospace Exploration Agency (JAXA), Kanagawa 252-5210, Japan
[2] Faculty of Science, Kanagawa University, 3-27-1 Rokukakubashi, Kanagawa-ku, Yokohama-shi, Kanagawa 221-8686, Japan
[3] Interdisciplinary Theoretical & Mathematical Science Program (iTHEMS), RIKEN, 2-1 Hirosawa, Wako, Saitama 351-0198, Japan
[4] Department of Physics, Ehime University, 2-5 Bunkyocho, Matsuyama, Ehime 790-8577, Japan
[5] Max-Planck-Institut für Kernphysik, P.O. Box 103980, D-69029 Heidelberg, Germany
[6] Department of Physics and Astronomy, University of Manitoba, Winnipeg, MB R3T 2N2, Canada
[7] Frontier Research Institute for Interdisciplinary Sciences, Tohoku University, Sendai 980-8578, Japan
[8] Astronomical Institute, Graduate School of Science, Tohoku University, Sendai 980-8578, Japan
[9] Departamento de Física, CUCEI, Universidad de Guadalajara, Blvd. Marcelino García Barragan 1420, Olímpica, 44430, Guadalajara, Jalisco, Mexico
[10] Instytut Fizyki Jądrowej PAN, ul. Radzikowskiego 152, 31-342 Kraków, Poland
[11] Columbia Astrophysics Laboratory, Columbia University, 538 West 120th Street, New York, NY 10027, USA
[12] Department of Physics, Michigan Technological University, Houghton, MI, USA
[13] Institute for Cosmic Ray Research, University of Tokyo, Kashiwa 277-8582, Japan
[14] Department of Physics, Graduate School of Science, The University of Tokyo, 7-3-1 Hongo, Bunkyo-ku, Tokyo 113-0033, Japan
[15] Faculty of Education, Shizuoka University, 836 Ohya, Suruga-ku, Shizuoka, Shizuoka 422-8529, Japan
[16] Konan University, Department of Physics, 8-9-1 Okamoto, Higashinada, Kobe, Hyogo, 658-8501, Japan
[17] Department of Physics, Graduate School of Science, Kyoto University, Kitashirakawa Oiwake-cho, Sakyo-ku, Kyoto 606-8502, Japan
[18] Department of Physics, University of Maryland, College Park, MD, USA
[19] Université Bordeaux, CNRS, CENBG, UMR 5797, F-33170 Gradignan, France
[20] Department of Physics, Tokyo University of Science, 1-3 Kagurazaka, Shinjuku-ku, Tokyo 162-8601, Japan
[21] Centre for Extragalactic Astronomy, Department of Physics, University of Durham, South Road, Durham DH1 3LE, UK
[22] Université Grenoble Alpes, CNRS, IPAG, F-38000 Grenoble, France
[23] Dipartimento di Matematica e Fisica, Universitá degli Studi RomaTre, Via della Vasca Navale 84, I-00146 Roma, Italy
[24] ESO, Karl-Schwarzschild-Strasse 2, 85748, Garching bei München, Germany
[25] Instituto de Astrofísica de Canarias, E-38205 La Laguna, Tenerife, Spain
[26] Departamento de Astrofísica, Universidad de La Laguna, E-38206 La Laguna, Tenerife, Spain
[27] Department of Earth and Space Science, Graduate School of Science, Osaka University, 1-1 Machikaneyama, Toyonaka, Osaka 560-0043, Japan
[28] Department of Astronomy, Kyoto University, Kitashirakawa-Oiwake-cho, Sakyo-ku, Kyoto, Kyoto 606-8502, Japan

Abstract

A recent report on the detection of very-high-energy gamma rays from V4641 Sagittarii (V4641 Sgr) up to ≈ 0.8 PeV has made it the second confirmed "PeVatron" microquasar. Here we report on the observation of V4641 Sgr with X-Ray Imaging and Spectroscopy Mission (XRISM) in 2024 September. Thanks to the large field of view and low background, the CCD imager Xtend successfully detected for the first time X-ray extended emission around V4641 Sgr with a significance of $\gtrsim 4.5\sigma$ and $>10\sigma$ based on our imaging and spectral analysis, respectively. The spatial extent is estimated to have a radius of $7' \pm 3'$ (13 ± 5 pc at a distance of 6.2 kpc) assuming a Gaussian-like radial distribution, which suggests that the particle acceleration site is within ~ 10 pc of the microquasar. If the X-ray morphology traces the diffusion of accelerated electrons, this spatial extent can be explained by either an enhanced magnetic field ($\sim 80\,\mu$G) or a suppressed diffusion coefficient ($\sim 10^{27}$ cm^2 s^{-1} at 100 TeV). The integrated X-ray flux, $(4\text{--}6) \times 10^{-12}$ erg s^{-1} cm^{-2} (2–10 keV), would require a magnetic field strength higher than the Galactic mean ($\gtrsim 8\,\mu$G) if the diffuse X-ray emission originates from synchrotron radiation and the gamma-ray emission is predominantly hadronic. If the X-rays are of thermal origin, the measured extension, temperature, and plasma density can be explained by a jet with a luminosity of $\sim 2 \times 10^{39}$ erg s^{-1}, which is comparable to the Eddington luminosity of this system.

Unified Astronomy Thesaurus concepts: Low-mass x-ray binary stars (939); Gamma-ray sources (633); Radio jets (1347); Non-thermal radiation sources (1119)

---

[29] Present affiliation: Institut d'Astrophysique de Paris, CNRS UMR 7095, Sorbonne Université, 98 bis bd Arago, F-75014 Paris, France.

1. Introduction

The origin of Galactic cosmic rays has been a long-standing question and is of increasing interest in recent years thanks to the growing high-sensitivity X-ray, gamma-ray, and neutrino observatories. Among the candidates for Galactic cosmic-ray
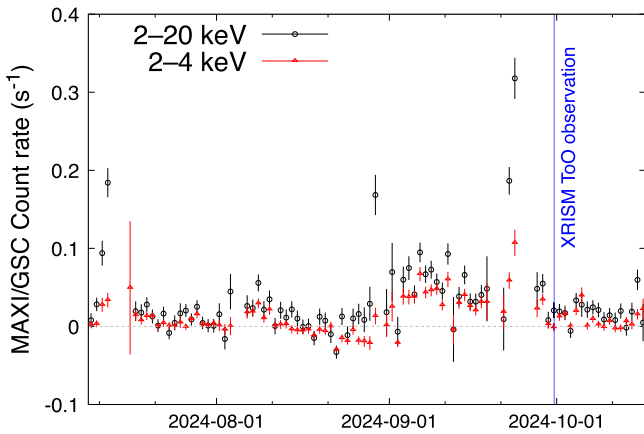
Figure 1. MAXI/GSC light curves of V4641 Sgr showing the bursting activity in 2024 September, obtained from http://maxi.riken.jp/star_data/J1819-254/ J1819-254.html. The observation period with XRISM is indicated with the blue transparent region.

accelerators, microquasars, where accreting black holes are powering jets, are an emerging class of Galactic PeVatrons after the TeV detection of the W50-SS433 system (A. U. Abeysekara et al. 2018; H.E.S.S. Collaboration et al. 2024). Most recently, LHAASO discovered gamma-ray emission exceeding 100 TeV from directions overlapping with several microquasars (LHAASO Collaboration 2024). The detection of gamma rays with $E > 100$ TeV suggests that parent particles (either protons or electrons) are accelerated beyond 1 PeV, indicating these microquasars are potential PeVatrons.

V4641 Sagittarii (V4641 Sgr) was found to exhibit extended gamma-ray emission up to ≈ 0.8 PeV in its surroundings, which is the brightest among the TeV-detected microquasars (R. Alfaro et al. 2024; LHAASO Collaboration 2024). V4641 Sgr is a low-mass X-ray binary consisting of a black hole with a mass of $6.4 \pm 0.6\, M_\odot$ and a B9III companion star with a mass of $2.9 \pm 0.4\, M_\odot$ (R. K. D. MacDonald et al. 2014), located at a distance of ≈ 6.2 kpc (R. K. D. MacDonald et al. 2014; P. Gandhi et al. 2019). In contrast to other microquasars, V4641 Sgr is characterized by violent X-ray outbursts, which include a rapid onset and exponential decay (M. Revnivtsev et al. 2002). The outbursts are observed once in ~ 2 yr without clear periodicity.[30] Radio observations with the Very Large Array, performed within 1 day after an X-ray burst in 1999, showed a luminous jetlike radio structure of about $0\overset{''}{.}25$ length (R. M. Hjellming et al. 2000), much more compact than the gamma-ray extension of $\approx 0\overset{\circ}{.}54$ (R. Alfaro et al. 2024).

In these months, V4641 Sgr is gaining even more attention because it has been exhibiting a bursting activity since 2024 September (Figure 1; report on MAXI/GSC observations, Negoro et al. 2024). Following other X-ray observatories such as Swift and XMM-Newton, the X-Ray Imaging and Spectroscopy Mission (XRISM; M. Tashiro et al. 2018, 2020, 2024) observed V4641 Sgr as a generic Target of Opportunity (ToO) observation. In this Letter, we report on a morphological and spectral analysis of the environment of V4641 Sgr and the detection of extended emission with XRISM.

2. Observation and Data Reduction

XRISM is equipped with the microcalorimeter Resolve (Y. Ishisaki et al. 2018) and wide field-of-view (FoV) CCD camera Xtend (K. Mori et al. 2022). In this work, we focus on the data obtained with Xtend to search for a possible extended emission.[31] Xtend provides a $\approx 38' \times 38'$ FoV for the energy range 0.4–13 keV with an energy resolution better than 200 eV (FWHM; K. Mori et al. 2024). The angular resolution is $< 1\overset{'}{.}7$ (half-power diameter, HPD; K. Tamura et al. 2024).

V4641 Sgr was observed with XRISM as a generic ToO target on 2024 September 30 UT (ObsID: 901001010). Since the allocated time for generic ToO observations is very limited, the observation duration was only ≈ 20 ks. We reduced the data with the pre-release Build 7 XRISM software with HEAsoft version 6.32 (HEASARC 2014) and calibration database (CALDB) version 8 (v20240815; M. Loewenstein et al. 2020; Y. Terada et al. 2021). We excluded periods of the Earth eclipse and sunlit Earth's limb, as well as passages of the South Atlantic Anomaly. The effective exposure of Xtend that remains after the standard data reduction is ≈ 12.2 ks. We removed flickering pixels[32] using the searchflickpix tool in addition to removing bad pixels and columns manually.

For the morphological analysis, we use the night-earth and day-earth occultation data collected from 2024 March 10 to July 31 from the XRISM trend archive (rev. 3).[33] The night-earth data are used to evaluate the event rate and spatial distribution of the particle background (non-X-ray background), whereas the day-earth data are used as a reference for the detector image from a uniform emission on the plane of the sky, which allows us to obtain the vignetting curve (effective area as a function of the off-axis angle).

In our spectral analysis, we use XSPEC version 12.13.1 (K. A. Arnaud 1996) with the C-statistic (W. Cash 1979), and AtomDB version 3.0.9 (A. R. Foster et al. 2012). Redistribution matrix files (RMFs) are created with the xtdrmf task using the cleaned event file and CALDB based on ground measurements. Auxiliary response files (ARFs) are generated with the xaarfgen task assuming constant surface-brightness emission because the sky background dominates the data. The errors given in the text and figures indicate 1σ confidence intervals.

3. Analysis and Results

3.1. X-Ray Morphology

Figures 2(a) and (b) show a 1.2–7.0 keV image with XRISM Xtend, indicating a hint of extended emission around V4641 Sgr. Here, events with lower and higher energies are excluded because of the significant contribution of the sky and particle background, respectively (see Section 3.2). To be more precise, we subtract the particle-background image extracted from the night-earth data set and scaled to match the 9.0–13.0 keV event rate, dominated by the particle background, of the V4641 Sgr observation. Then we also correct for the vignetting of the mirror assembly using the day-earth image. As a result, we obtain Figure 2(c), which shows extended emission around V4641 Sgr.

---

[30] Refer to, e.g., a light curve by MAXI (http://maxi.riken.jp/star_data/ J1819-254/J1819-254.html).

[31] The results of the high-resolution spectroscopy of V4641 Sgr itself with Resolve will be reported separately (M. Shidatsu et al. 2024, in preparation).
[32] Pixels with anomalously high event rates, which mostly record pseudo-events at $\lesssim 1$ keV (H. Nakajima et al. 2018).
[33] https://data.darts.isas.jaxa.jp/pub/xrism/data/trend/rev3/

(a) XRISM/Xtend 1.2–7.0 keV image　　　(b) XRISM/Xtend 1.2–7.0 keV image　　　(c) NXB-subtracted, vignetting-corrected
　　　　　　　　　　　　　　　　　　　　　　　(with coarse binning)　　　　　　　　1.2–7.0 keV image with HAWC contours
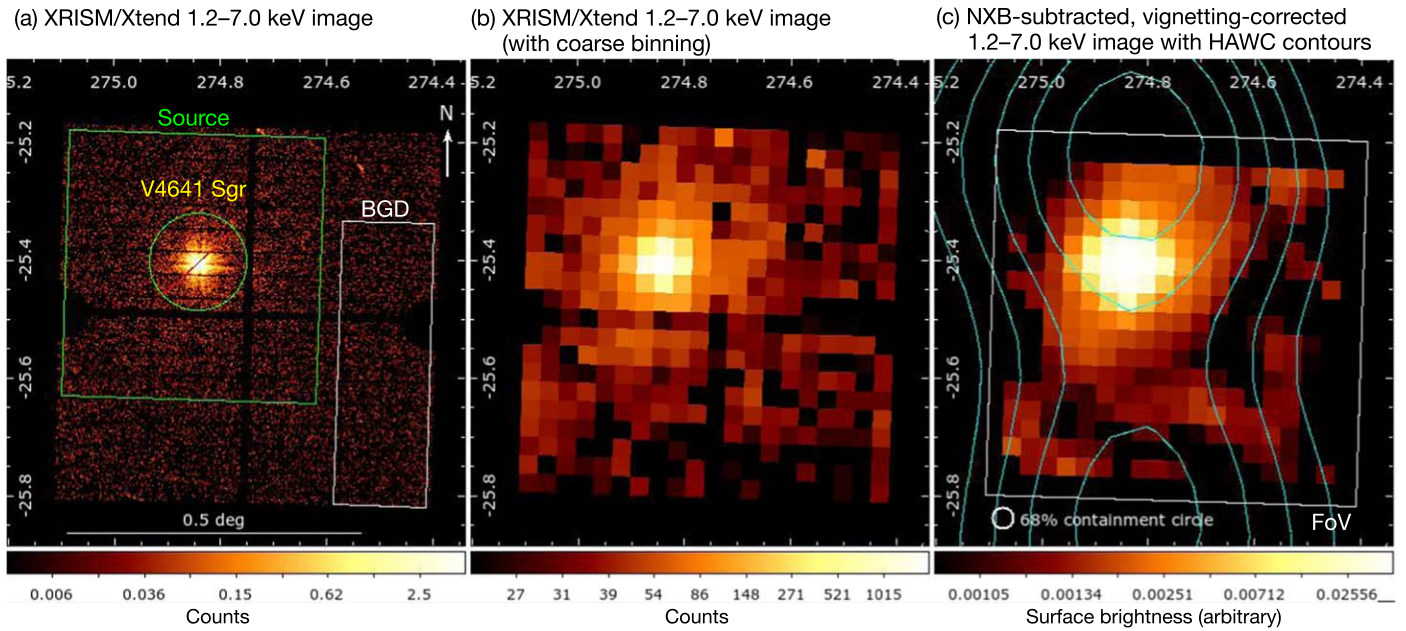

Figure 2. (a) A 1.2–7.0 keV XRISM Xtend image with the regions for the spectral analysis. (b) Same with a course binning. (c) The image after the particle-background subtraction and vignetting correction and with the HAWC gamma-ray contours (>1 TeV; R. Alfaro et al. 2024) and the Xtend field of view (FoV) overlaid. The 68% containment circle of the point-spread function at 6.4 keV is shown as a reference. The images are shown on the Equatorial coordinates (J2000).

In order to quantify the spatial extent of the extended emission, we extract a one-dimensional radial profile centered at V4641 Sgr (Figure 3). The profile is extracted from a circle with a radius of 12′ and from a partial annulus extending from 12′ to 24′ (Figure 3(a)). The location of the partial annulus is chosen to extend to the region where events are dominated by particle background. The radial profile for the emission of V4641 Sgr (point-spread function, PSF) is made with a ray-tracing simulation using the xrtraytrace task at 6–7 keV.[34] The morphology of the sky background, which should originate from a nearly uniform emission on the plane of the sky, is modeled using the day-earth image, which is equivalent to the vignetting image. The radial profile of the particle background is extracted from the night-earth data set. As for the the extended emission, we assume a Gaussian-like distribution as a simple model. We model the radial profile from the 1.2–7.0 keV image with the empirical model "(V4641 Sgr) + (extended emission) + (sky background) + (particle background)." The free parameters include the normalizations of the components of V4641 Sgr, the extended emission, and sky background, and the width of the extended emission (Gaussian function). We employ a least chi-square fit to determine the best-fit parameters and their confidence intervals. The best-fit model is shown in Figure 3(b). We obtain the best-fit Gaussian σ width of the extended-emission model of $7' \pm 3'$, which is converted to 13 ± 5 pc at a distance of 6.2 kpc. The model without the extended emission does not fit the data in the radii of $\approx 5'$–12′ (Figure 3(b)). The detection significance can be evaluated from the fit statistics with and without the extended-emission model using the F-test, to be $\gtrsim 4.5\sigma$ (F-test probability of $< 8.8 \times 10^{-6}$) taking into account the upper limits of the systematic uncertainties described below.

We evaluate the impact of the systematic uncertainties associated with the PSF tail: <80% within the radii <8′ (K. Tamura et al. 2022, 2024), off-axis effective area: <30%, and particle-background level: <5% (H. Uchida et al. 2024, in preparation). These uncertainty levels are also shown in Figure 3(b). These systematic uncertainties can alter the flux of the emission up to ≈30%.

3.2. X-Ray Spectra

In the next step, we examine the X-ray spectrum of the extended emission marginally detected in Section 3.1. The source and background (BGD) regions are defined as shown in Figure 2(a). The source region encloses most of the apparent extended emission found in the morphological analysis (Section 3.1) but without the contribution of V4641 Sgr itself.[35] The BGD region is nearly free from the extended emission (Figure 2(c)). We only use the energies above 1.0 keV, where the contamination from potential flickering pixels and bad pixels remaining after data reduction is negligible.

For the spectral model, we consider the sky and particle background in addition to the extended source. As for the sky background, we apply the foreground emission (Local Hot Bubble), Milky Way halo (transabsorption emission), and cosmic X-ray background (CXB). The former two are modeled with the apec model in XSPEC with the electron temperatures of 0.1 keV and 0.6 keV, respectively, and the solar abundance (K. D. Kuntz & S. L. Snowden 2008; K. Masui et al. 2009; M. C. H. Yeung et al. 2024). The uncertain Galactic absorption for the Milky Way halo component is not considered because it does not strongly affect the energy range we focus on. Only their fluxes are treated as free parameters. As for CXB, we use the power-law model with a photon index of 1.41 and the 2–10 keV flux fixed to 5.4×10^{-15} erg cm^{-2} arcmin^{-2} (A. Kushino et al. 2002). The Galactic absorption is considered with the

---

[34] The in-orbit calibration of the PSF has been done best for this energy range. The energy dependence of the PSF in 1.2–7.0 keV (<80% at radii smaller than 8′; K. Tamura et al. 2022) is included in the systematic uncertainty considered later.

[35] $\lesssim$3% of the total flux remains within the source region (K. Tamura et al. 2024), which is lower than the sky-background level.

(a) XRISM/Xtend 1.2–7.0 keV image with radial-profile extraction region
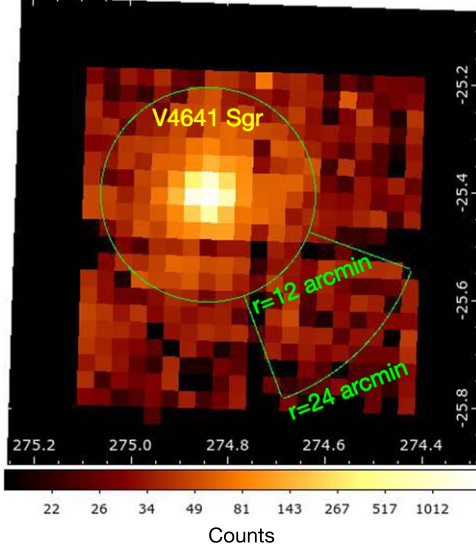
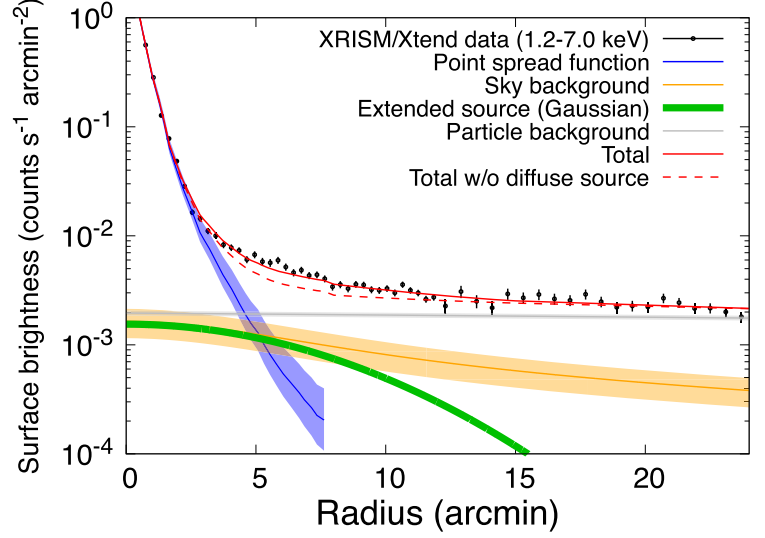## (b) 1.2–7.0 keV radial profile and best-fit models

Figure 3. (a) A 1.2–7.0 keV XRISM Xtend image with the radial-profile extraction region centered at V4641 Sgr (green). (b) Extracted radial profile with the models for the point-spread function at 6.4 keV, sky background, particle background, and extended emission modeled with a Gaussian function. The transparent regions indicate the systematic uncertainty ranges (see the text for details).

(a) X-ray spectrum and best-fit models
(extended emission ignored in BGD region)
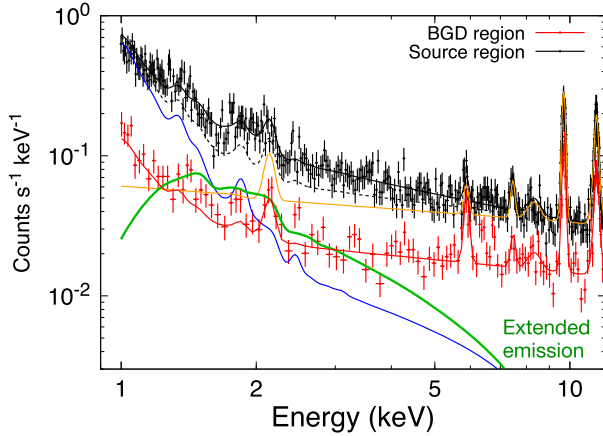
(b) X-ray spectrum and best-fit models
(extended emission considered in BGD region)
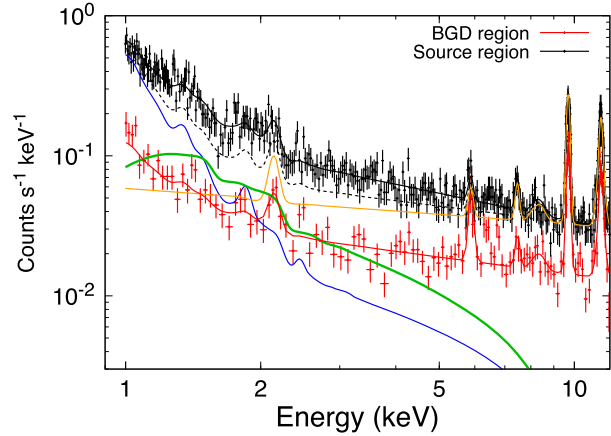
Figure 4. (a) X-ray spectra obtained with XRISM Xtend and the best-fit spectral models in the case where contamination of the extended emission in the BGD region is ignored and (b) assumed to be 10% in flux of the source region. The green, blue, and orange solid lines indicate the extended emission, sky background, and particle background, respectively, for the source region. The black and red solid lines indicate the total models for the source and BGD regions, respectively. The black dashed line is the total model for the source region but without the extended-emission component.

tbabs model with a column density of 1.6×10^{21} cm^{-2} (J. Wilms et al. 2000; HI4PI Collaboration et al. 2016).

The particle-background model is developed from the night-earth observation data. The extracted spectrum can be explained with a model composed of the fluorescence lines of Au-M, Ni-K, and Au-L and a continuum (power law; H. Nakajima et al. 2018; H. Uchida et al. 2024, in preparation). As the particle-background level depends on the satellite position and solar activity but without changing the spectral shape significantly ($\lesssim 10\%$; H. Uchida et al. 2024, in preparation), we apply this spectral model to the V4641 Sgr observation. Only the total normalization is treated as a free parameter.

As for the extended emission, we first use an absorbed power-law model (tbabs × powerlaw). In the spectral modeling, we fit the spectra of the source and BGD simultaneously with two assumptions: (a) the extended emission does not contaminate the BGD region and (b) 10% flux of the extended emission in the source region contributes to the BGD region. The contamination level of 10% is derived by evaluating the integrals of a Gaussian function for the extended source, assuming a σ of $10'$ (best-fit value plus 1σ error; see Section 3.1) over the source and BGD regions. In the spectral modeling, we find that the detector gain is slightly shifted from that expected by the RMFs due to the degradation on orbit in ~1 yr. We thus correct the gain slopes of the RMFs

Table 1
Best-fit Spectral Parameters of the Extended Emission

Case (a)	$N_{\rm H}$ (10^{22} cm^{-2})	1.8 ± 0.5
	Power-law index	2.4 ± 0.3
	Power-law flux (2–10 keV) (10^{-15} erg s^{-1} cm^{-2} arcmin^{-2})	7.8 ± 0.9
	Integrated power-law flux (2–10 keV)[a] (10^{-12} erg s^{-1} cm^{-2})	4.3 ± 0.5
	C-stat./d.o.f.	4190.1/3658
Case (b)	$N_{\rm H}$ (10^{22} cm^{-2})	0.6 ± 0.4
	Power-law index	1.8 ± 0.2
	Power-law flux (2–10 keV) (10^{-15} erg s^{-1} cm^{-2} arcmin^{-2})	9.2 ± 1.1
	Integrated power-law flux (2–10 keV)[a] (10^{-12} erg s^{-1} cm^{-2})	5.1 ± 0.6
	C-stat./d.o.f.	4147.6/3658
Case (c)	$N_{\rm H}$ (10^{22} cm^{-2})	1.5 ± 0.4
	$kT_{\rm e}$ (keV)	3.2 ± 0.7
	$n_{\rm e}n_{\rm p}V$ (10^{58} cm^{-3})	1.3 ± 0.2
	C-stat./d.o.f.	4192.3/3658

Note.
[a] Integrated flux for the source region, which has an area of 629.4 arcmin^2.

by ≈0.3% and ≈0.2% for the source and BGD regions, respectively, to fit the detector background lines.

Figure 4 shows the results corresponding to the two cases (a) and (b). We obtain the fit statistics C-stat./d.o.f. = 4190.1/3658 and 4147.6/3658, respectively. The case (b) better explains the observations. The best-fit spectral parameters of the extended emission are summarized in Table 1. The unabsorbed flux in 2–10 keV is determined to be ≈7–10 × 10^{-15} erg s^{-1} cm^{-2} arcmin^{-2}. The spectral index is found to depend on the assumptions strongly, and thus is not constrained well. The detection significance of the extended emission can be evaluated, from the fit statistics with and without the extend-emission model using the likelihood ratio test (for the C-statistic), to be >10σ (ΔC = 361.9 and Δd.o.f. = 3).

To account for the possibility that the emission is of thermal origin, we also assume a thermal emission model (case (c)). If a collisional ionization equilibrium plasma model (apec) with the solar abundance (J. Wilms et al. 2000) and with free electron temperature and normalization replaces the power-law model of the case (a), we obtain the fit statistics C-stat/d.o.f. = 4192.3/3658. This is similar to the result of the case (a). The derived parameters are shown in Table 1. The electron temperature $kT_{\rm e}$ is constrained to be 3.2 ± 0.7 keV. The unabsorbed flux in 2–10 keV is estimated to be (7 ± 1) × 10^{-15} erg s^{-1} cm^{-2} arcmin^{-2}. Based on the volume emission measure $n_{\rm e}n_{\rm p}V$, where $n_{\rm e}$, $n_{\rm p}$, and V, respectively, are the electron density, proton density, and volume, one can derive the plasma density ≈0.3 cm^{-3} $(r/10$ pc$)^{-1.5}$, with r being the radius of the spherical plasma.

Considering its location (ℓ = 6°.77 and b = −4°.79) close to the Galactic center, the spectrum is possibly affected by the Galactic ridge X-ray emission (GRXE; H. Uchiyama et al. 2013; S. Yamauchi et al. 2016), but the exact contribution at such high Galactic altitudes is quite uncertain. So, we add a GRXE model (with the spectral shape described in Table 3 of H. Uchiyama et al. 2013) with the highest flux level allowed from the best-fit radial-profile models (Section 3.1).[36] As a

result, the spectral excess is still found to be significant with a ≈9σ significance with a somewhat reduced flux of (3.6 ± 0.8) × 10^{-15} erg s^{-1} cm^{-2} arcmin^{-2} in 2–10 keV.

4. Discussion and Conclusion

We have found extended X-ray emission around V4641 Sgr. The derived extension of ∼20 pc assuming a Gaussian-like radial profile is smaller than that seen in gamma rays (≈60 pc with the HAWC observation; R. Alfaro et al. 2024). Here we first discuss the nature of the acceleration environment with an assumption that the X-rays are of nonthermal origin. Although we cannot confidently identify the exact site of particle acceleration, the X-ray radial profile describable with a Gaussian function centered at V4641 Sgr suggests that the acceleration site is close to the microquasar ($\lesssim$10 pc). The synchrotron cooling timescale for X-ray-emitting electrons is $t_{\rm cool}$ ≈ 1000 yr $(E_{\rm e}/100$ TeV$)^{-1}(B/10$ μG$)^{-2}$, where the $E_{\rm e}$ and B are the electron energy and magnetic field strength, respectively. The diffusion length for this timescale is $R_{\rm dif} \approx (4D(100$ TeV$)t_{\rm cool})^{0.5}$ ≈80 pc $(D(100$ TeV$)/5 \times 10^{29}$ cm^2 s$^{-1})^{0.5}(E_{\rm e}/100$ TeV$)^{-0.5}$ $(B/10$ μG$)^{-1}$, where $D(E_{\rm e})$ is the diffusion coefficient. Thus, electrons with energies ≈100 TeV can travel within the X-ray-emitting region, if we assume the Galactic mean value for $D(E_{\rm e}) = 2 \times 10^{28}$ cm^2 s^{-1} $(E_{\rm e}/3$ GeV$)^{\delta}$ with δ = 0.3–0.6 (V. Berezinskii et al. 1990; V. S. Ptuskin et al. 2006). To match the observed X-ray extent $R_{\rm dif}$ ≈ 10 pc, either an enhanced magnetic field B ≈ 80 μG with $D(E_{\rm e}) = 2 \times 10^{28}$ cm^2 s^{-1} $(E_{\rm e}/3$ GeV$)^{0.3}$ or a suppressed diffusion coefficient $D(100$ TeV$) \approx 1 \times 10^{27}$ cm^2 s^{-1} with an interstellar magnetic field level B ≈ 3 μG is required.

Given that the very-high-energy gamma-ray emission is likely hadronic due to the very hard spectra with Γ = 2.2 ± 0.2 (R. Alfaro et al. 2024; LHAASO Collaboration 2024), one can constrain the lower limit of the magnetic field strength based on the highest allowed level of the inverse Compton gamma-ray flux. As shown in Figure 5, we obtain $B \gtrsim 8$ μG, which indicates that the magnetic field is likely enhanced compared with the interstellar values. Since the spectral shape of accelerated electrons is completely unknown, we assume a cutoff power-law model and have examined various parameter sets, with an index of 2–3 and a cutoff energy of 10–100 TeV. Radiation cooling is also taken into consideration, as the X-ray spectrum is extracted from the region extending beyond $R_{\rm dif}$ (Figures 2 and 3), where electrons may be affected by cooling. In conclusion, the choice of the parameters and the cooling effect does not significantly affect the lower limit of ≈8 μG.

If the X-ray emission is of thermal origin, one can discuss the physical process that produced the thermal plasma based on the electron temperature and plasma density. Assuming a shock heating as a representative scenario to generate X-ray emitting plasma in interstellar space, the derived electron temperature ≈3 keV would require a shock velocity $\gtrsim$1500 km s^{-1} (Y. Ohshiro et al. 2024; XRISM Collaboration 2024). Plasma density ∼0.3 cm^{-3} is typical for the interstellar medium. A supernova remnant would be able to explain these parameters, but the age estimate for the black hole in this system, $\gtrsim$10 Myr (G. Salvesen & S. Pokawanvit 2020), would contradict this scenario. Thus, a shock originating from black hole activities, e.g., a jet termination shock, would be more feasible. If we assume a pair of jets along the line-of-sight direction (R. M. Hjellming et al. 2000; J. A. Orosz et al. 2001), strong and adiabatic shock, and homogeneous plasma, the jet luminosity can be estimated from the shock kinetic energy as $L_{\rm jet} \sim 2 \times 10^{39}$ erg s^{-1} $(n_{\rm ISM}/0.08$ cm$^{-3})(v_{\rm jet}/1500$ km s$^{-1})^3(R/10$ pc$)^2$,

---

[36] Total sky-background rate of ≈70% particle-background rate in 1.2–7.0 keV for radii of 5′–15′, roughly corresponding to the source region.
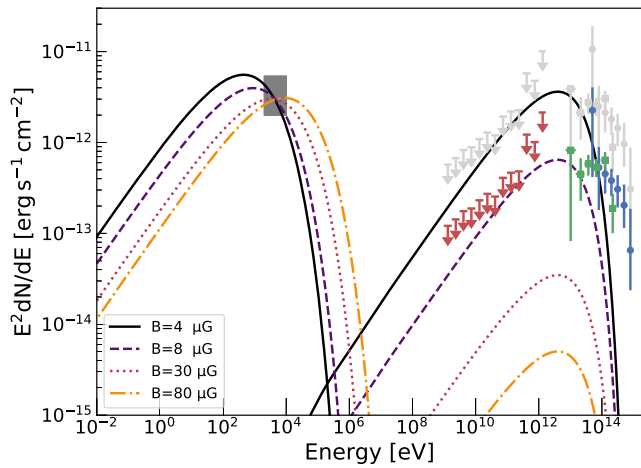
Figure 5. Broadband spectral energy distribution. The X-ray flux is derived for the XRISM source region (Figure 2(a)). The red, green, and blue flux points indicate gamma-ray spectra by Fermi-LAT, HAWC, and LHAASO (R. Alfaro et al. 2024; LHAASO Collaboration 2024; A. Neronov et al. 2024), respectively, scaled to the XRISM source region, while the gray points show spectra from the entire gamma-ray-emitting region. Synchrotron and inverse Compton models with various magnetic field strengths are overlaid, assuming electrons with a power-law index of 2 and a cutoff energy of 50 TeV. The total energy content in electrons ($E > 1$ TeV) is 2.6×10^{47}, 4.7×10^{46}, 2.5×10^{45}, and 3.6×10^{44} erg for $B = $ 4, 8, 30, and 80 μG, respectively.

where $n_{\rm ISM}$, $v_{\rm jet}$, and R are the interstellar plasma density, jet velocity, and radius of the extended emission, respectively. This is comparable to the Eddington luminosity of the system (R. K. D. MacDonald et al. 2014; P. Gandhi et al. 2019). This luminosity would not be unrealistic as the jet luminosity during the outburst in 1999 was inferred to exceed 10^{39} erg s^{-1} (M. Revnivtsev et al. 2002). The spatial extent of the lobe produced by the jet to explain the observed extended X-rays, $\gtrsim 20$ pc, would be much larger than the typical size of the radio lobes found in microquasars such as Circinus X-1, Cygnus X-1, and GRS 1758−258 ($\lesssim 5$ pc; see a review by E. Gallo 2010), but would be comparable to the X-ray extension of the SS 433/W50 complex (~ 30 pc; S. Safi-Harb et al. 2022). Such a large spatial extent may be related to the inferred high jet luminosity. R. Alfaro et al. (2024) suggests that a jet with a luminosity of 10^{39} erg s^{-1} can, in principle, explain the extension of the TeV emission around V4641 Sgr (≈ 60 pc).

An alternative origin to the extended X-ray emission around V4641 Sgr could be a dust-scattering halo. The flux of the scattered photons can be evaluated based on the relation between an interstellar absorption column and optical depth in scattering (P. Predehl & J. H. M. M. Schmitt 1995), the absorption column density $\approx 1.6 \times 10^{21}$ cm^{-2}, and a typical flux of V4641 Sgr during the bursting activity from 2024 September, $\sim 10^{-11}$–10^{-10} erg s^{-1} cm^{-2}.[37] The resultant flux level for the source region, $< 10^{-13}$ erg s^{-1} cm^{-2} in 2–4 keV, is lower than the sky background. We have also examined 25 ks archival Chandra data in 2002 (ObsID: 3800), which were obtained during its quiescence (~ 5 months after the outburst in 2002 May) with a low flux of V4641 Sgr $\sim 10^{-12}$ erg s^{-1} cm^{-2}.[38] With the same source and sky-background spectral models

as case (a) (Section 3.2) plus a particle-background model for Chandra ACIS (H. Suzuki et al. 2021), we obtained a surface brightness of the excess source, $\sim 7 \times 10^{-15}$ erg s^{-1} cm^{-2} arcmin^{-2} in 2–10 keV, similar to that obtained with XRISM. This supports the idea that the extended emission is more persistent and thus independent of the bursting activity of V4641 Sgr. To conclude, it is unlikely that the observed extended X-rays are due to dust scattering, without specific conditions such as the presence of dense clumps in the line of sight.

This work has discovered for the first time extended emission around V4641 Sgr with XRISM Xtend. The spatial extent of the X-ray emission ~ 20 pc in diameter is smaller than that seen in gamma rays. Assuming that the X-rays are of nonthermal origin, this suggests that the X-rays originate from an electron population near the acceleration sites, which is different from that responsible for the gamma-ray emission. If the X-rays are of thermal origin, a jet termination shock would be able to explain the measured properties with a jet luminosity $\sim 2 \times 10^{39}$ erg s^{-1}, which is comparable to the Eddington luminosity of this system. Future radio observations and more extensive X-ray observations of the gamma-ray-emitting region will help disentangle the nature of the acceleration environment.

ORCID iDs

Hiromasa Suzuki https://orcid.org/0000-0002-8152-6172
Naomi Tsuji https://orcid.org/0000-0001-7209-9204
Yoshiaki Kanemaru https://orcid.org/0000-0002-4541-1044
Megumi Shidatsu https://orcid.org/0000-0001-8195-6546
Laura Olivera-Nieto https://orcid.org/0000-0002-9105-0518
Samar Safi-Harb https://orcid.org/0000-0001-6189-7665
Shigeo S. Kimura https://orcid.org/0000-0003-2579-7266
Eduardo de la Fuente https://orcid.org/0000-0001-9643-4134
Sabrina Casanova https://orcid.org/0000-0002-6144-9122
Kaya Mori https://orcid.org/0000-0002-9709-5389
Xiaojie Wang https://orcid.org/0000-0001-6798-353X

---

[37] See, e.g., the report on MAXI/GSC observations in 2024 September (Negoro et al. 2024) and XRISM results by M. Shidatsu et al. (2024, in preparation).

[38] Note that this observation covered a limited region where one cannot obtain a background region free from the extended source according to the extension measured with XRISM. Thus it is hard to detect the extended emission with this Chandra observation alone.

Sei Kato ⓘ https://orcid.org/0000-0003-2251-2544
Dai Tateishi ⓘ https://orcid.org/0000-0003-0248-4064
Hideki Uchiyama ⓘ https://orcid.org/0000-0003-4580-4021
Takaaki Tanaka ⓘ https://orcid.org/0000-0002-4383-0368
Hiroyuki Uchida ⓘ https://orcid.org/0000-0003-1518-2188
Shun Inoue ⓘ https://orcid.org/0000-0003-3085-304X
Dezhi Huang ⓘ https://orcid.org/0000-0002-5447-1786
Marianne Lemoine-Goumard ⓘ https://orcid.org/0000-0002-4462-3686
Daiki Miura ⓘ https://orcid.org/0009-0009-0439-1866
Shoji Ogawa ⓘ https://orcid.org/0000-0002-5701-0811
Shogo B. Kobayashi ⓘ https://orcid.org/0000-0001-7773-9266
Chris Done ⓘ https://orcid.org/0000-0002-1065-7239
Maxime Parra ⓘ https://orcid.org/0009-0003-8610-853X
Maria Díaz Trigo ⓘ https://orcid.org/0000-0001-7796-4279
Teo Muñoz-Darias ⓘ https://orcid.org/0000-0002-3348-4035
Montserrat Armas Padilla ⓘ https://orcid.org/0000-0002-4344-7334
Ryota Tomaru ⓘ https://orcid.org/0000-0002-6797-2539
Yoshihiro Ueda ⓘ https://orcid.org/0000-0001-7821-6715

References

Abeysekara, A. U., Albert, A., Alfaro, R., et al. 2018, Natur, 562, 82
Alfaro, R., Alvarez, C., Arteaga-Velázquez, J., et al. 2024, Natur, 634, 557
Arnaud, K. A. 1996, in ASP Conf. Ser. 101, XSPEC: The First Ten Years, ed. G. H. Jacoby & J. Barnes (San Francisco, CA: ASP), 17
Berezinskii, V., Bulanov, S., Ginzburg, V., Dogiel, V., & Ptuskin, V. 1990, Cosmic Ray Astrophysics (Amsterdam: North-Holland),
Cash, W. 1979, ApJ, 228, 939
Foster, A. R., Ji, L., Smith, R. K., & Brickhouse, N. S. 2012, ApJ, 756, 128
Gallo, E. 2010, in The Jet Paradigm, Lecture Notes in Physics, Vol. 794, ed. T. Belloni (Berlin: Springer), 85
Gandhi, P., Rao, A., Johnson, M. A. C., Paice, J. A., & Maccarone, T. J. 2019, MNRAS, 485, 2642
HEASARC, 2014 HEAsoft: Unified Release of FTOOLS and XANADU, Astrophysics Source Code Library, ascl:1408.004

H.E.S.S. Collaboration, Aharonian, F., Ait Benkhali, F., et al. 2024, Sci, 383, 402
HI4PI Collaboration, Ben Bekhti, N., Flöer, L., et al. 2016, A&A, 594, A116
Hjellming, R. M., Rupen, M. P., Hunstead, R. W., et al. 2000, ApJ, 544, 977
Ishisaki, Y., Ezoe, Y., Yamada, S., et al. 2018, JLTP, 193, 991
Kuntz, K. D., & Snowden, S. L. 2008, A&A, 478, 575
Kushino, A., Ishisaki, Y., Morita, U., et al. 2002, PASJ, 54, 327
LHAASO Collaboration 2024, arXiv:2410.08988
Loewenstein, M., Hill, R. S., Holland, M. P., et al. 2020, Proc. SPIE, 11444, 114445D
MacDonald, R. K. D., Bailyn, C. D., Buxton, M., et al. 2014, ApJ, 784, 2
Masui, K., Mitsuda, K., Yamasaki, N. Y., et al. 2009, PASJ, 61, S115
Mori, K., Tomida, H., Nakajima, H., et al. 2022, Proc. SPIE, 12181, 121811T
Mori, K., Tomida, H., Nakajima, H., et al. 2024, Proc. SPIE, 13093, 130931I
Nakajima, H., Maeda, Y., Uchida, H., et al. 2018, PASJ, 70, 21
Negoro, H., Nakajima, M., Fujiwara, K., et al. 2024, ATel, 16804
Neronov, A., Oikonomou, F., & Semikoz, D. 2024, arXiv:2410.17608
Ohshiro, Y., Suzuki, S., Okada, Y., Suzuki, H., & Yamaguchi, H. 2024, ApJ, 976, 180
Orosz, J. A., Kuulkers, E., van der Klis, M., et al. 2001, ApJ, 555, 489
Predehl, P., & Schmitt, J. H. M. M. 1995, A&A, 293, 889
Ptuskin, V. S., Moskalenko, I. V., Jones, F. C., Strong, A. W., & Zirakashvili, V. N. 2006, ApJ, 642, 902
Revnivtsev, M., Gilfanov, M., Churazov, E., & Sunyaev, R. 2002, A&A, 391, 1013
Safi-Harb, S., Mac Intyre, B., Zhang, S., et al. 2022, ApJ, 935, 163
Salvesen, G., & Pokawanvit, S. 2020, MNRAS, 495, 2179
Suzuki, H., Plucinsky, P. P., Gaetz, T. J., & Bamba, A. 2021, A&A, 655, A116
Tamura, K., Hayashi, T., Boissay-Malaquin, R., et al. 2022, Proc. SPIE, 12181, 121811V
Tamura, K., Hayashi, T., Boissay-Malaquin, R., et al. 2024, Proc. SPIE, 13093, 130931M
Tashiro, M., Maejima, H., Toda, K., et al. 2018, Proc. SPIE, 10699, 1069922
Tashiro, M., Maejima, H., Toda, K., et al. 2020, Proc. SPIE, 11444, 1144422
Tashiro, M., Watanabe, S., Maejima, H., et al. 2024, Proc. SPIE, 13093, 130931G
Terada, Y., Holland, M., Loewenstein, M., et al. 2021, JATIS, 7, 037001
Uchiyama, H., Nobukawa, M., Tsuru, T. G., & Koyama, K. 2013, PASJ, 65, 19
Wilms, J., Allen, A., & McCray, R. 2000, ApJ, 542, 914
XRISM Collaboration 2024, PASJ, 76, 1186
Yamauchi, S., Nobukawa, K. K., Nobukawa, M., Uchiyama, H., & Koyama, K. 2016, PASJ, 68, 59
Yeung, M. C. H., Ponti, G., Freyberg, M. J., et al. 2024, A&A, 690, A399